

See discussions, stats, and author profiles for this publication at: <https://www.researchgate.net/publication/244484764>

Study of Morphological and Related Properties of Aligned Zinc Oxide Nanorods Grown by Vapor Phase Transport on Chemical Bath Deposited Buffer Layers

ARTICLE *in* CRYSTAL GROWTH & DESIGN · OCTOBER 2011

Impact Factor: 4.89 · DOI: 10.1021/cg200977n

CITATIONS

17

READS

14

7 AUTHORS, INCLUDING:



Daragh Joseph Byrne

Dublin City University

17 PUBLICATIONS 132 CITATIONS

SEE PROFILE



Teresa Ben

Universidad de Cádiz

70 PUBLICATIONS 668 CITATIONS

SEE PROFILE



David González Robledo

Universidad de Cádiz

126 PUBLICATIONS 750 CITATIONS

SEE PROFILE



Martin Henry

Dublin City University

126 PUBLICATIONS 1,214 CITATIONS

SEE PROFILE

Study of Morphological and Related Properties of Aligned Zinc Oxide Nanorods Grown by Vapor Phase Transport on Chemical Bath Deposited Buffer Layers

Daragh Byrne,^{*,†} Rabie Fath Allah,[‡] Teresa Ben,[‡] David Gonzalez Robledo,[‡] Brendan Twamley,[§] Martin O. Henry,[†] and Enda McGlynn[†]

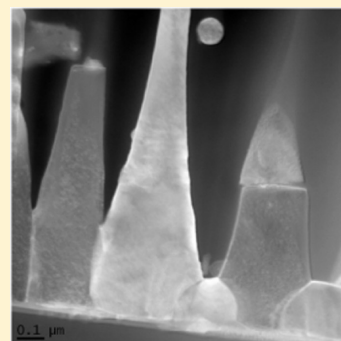
[†]School of Physical Sciences, National Centre for Plasma Science and Technology, Dublin City University, Glasnevin, Dublin 9, Ireland

[‡]Departamento Ciencia de los Materiales e Ingeniería Metalúrgica y Química Inorgánica, Facultad de Ciencias, Universidad de Cádiz, 11510 Puerto Real, Cádiz, Spain

[§]School of Chemical Sciences, Dublin City University, Glasnevin, Dublin 9, Ireland

S Supporting Information

ABSTRACT: *c*-axis aligned ZnO nanorods were deposited by vapor phase transport on textured chemical bath deposited buffer layers. In this work, we examine the role of the buffer layer and how it influences the vapor phase transport deposition process using both scanning and transmission electron microscopes and related techniques. Vapor phase transport deposition on chemical bath deposited buffer layers is a complex growth process with many simultaneously occurring effects including (i) substantial morphological transformation at high temperature, which influences the base of the nanorods; (ii) the formation of a mixed amorphous/crystalline $\text{Zn}_x\text{Si}_{1-x}\text{O}_y$ interface during the vapor phase transport growth on silicon substrates; (iii) the overgrowth of the ZnO seed layers by the silica interface rendering them inactive for nanorod nucleation, suggesting there is a minimum critical thickness ZnO buffer layer necessary for vapor phase transport growth of ZnO nanorods on silicon substrates. We discuss the relative importance of these effects on the overall growth process and use this understanding to explain previous results in the literature.



1. INTRODUCTION

Zinc oxide has in the past decade come to the forefront of materials research owing to its favorable electronic, optical, and chemical properties and because it is of considerable interest for many applications.^{1–7} For many of these applications, nanorods and nanowires are the preferred crystal morphology as they present significant advantages over bulk material or polycrystalline films. Consequently, there have been numerous reports on the growth of ZnO nanorods, both as unoriented and aligned arrays normal to the substrate, using a variety of techniques.^{8–14} Vapor phase transport (VPT) is a successful approach to deposit such high quality aligned arrays, typically employing epitaxially matched substrates with a catalyst or directly onto previously formed *c*-axis textured ZnO buffer layers. Detailed studies on the role of the ZnO buffer layers during VPT deposition have previously been reported. These works concentrated specifically on ZnO buffer layers prepared by pulsed laser deposition (PLD), magnetron sputtering, thermal oxidation of zinc films, electron beam evaporation, and molecular organic chemical vapor deposition (MOCVD).^{15–17}

Recently, it has been shown that *c*-axis aligned ZnO nanorod arrays can be grown by VPT on nonepitaxially matched substrates using chemical bath deposited (CBD) derived buffer layers.^{18–20} While in principle this approach is similar to that using the buffer

layers discussed above, it offers distinct advantages, in that relatively little specialized equipment and processes are necessary. This method combines CBD methods to create a thin (~ 200 – 300 nm) *c*-axis aligned nanorod buffer layer which is suitably robust for VPT deposition.²⁰

While in practice the VPT growth of aligned nanorods on a CBD derived buffer layer is a facile process, there are few reports, as far as we are aware, on the specific mechanisms that influence this process. In this work we focus on the structural and compositional changes during the VPT deposition of aligned nanorods on CBD derived buffer layer using silicon substrates, as silicon represents the most important nonepitaxially matched substrate for device applications. As will be seen, there are numerous factors that influence the final ZnO nanorod array, such as the density and thickness of the nanorod buffer layer or the temperature ramp rate of the furnace of the VPT process. In addition, we also analyze in detail the morphological changes and partial degradation of the underlying buffer layer during the high temperature deposition.

Received: July 28, 2011

Revised: October 3, 2011

Published: October 04, 2011

2. EXPERIMENTAL SECTION

ZnO nanorods were grown on silicon using a three-step process, combining chemical solution seeding, chemical bath deposition, and vapor phase transport. The growth methods are described in the Supporting Information and more details can be found in refs 19 and 20. Sample morphology was characterized by scanning electron microscopy (SEM; Karl-Zeiss EVO series) and field emission SEM (FE-SEM; Hitachi S5500). Conventional transmission electron microscopy (TEM) and high resolution TEM (HRTEM) were carried out in a JEOL 1200 EX and a 2010F microscope operating at 120 and 200 kV, respectively. Sample structure and composition was studied by high angle annular dark field scanning TEM (HAADF-STEM), electron dispersive X-ray spectroscopy (EDS), and electron energy loss spectroscopy (EELS), the last by using a Gatan imaging filter (GIF) camera. The samples were prepared for TEM studies both by a classical cross-section method using mechanical and ion milling processes and by a scraping method where the nanorod mass is removed from the substrate, dispersed, and dropped on a TEM grid.

3. RESULTS AND DISCUSSION

The growth process reported here is divided into three distinct stages as described in detail in the Supporting Information (experimental section part 1). First, a thin seed layer is formed on the substrate by drop coating an ethanolic zinc acetate solution followed by annealing. Second, a thin columnar film is grown on this seed layer by CBD, and last, well aligned ZnO nanorods are deposited by VPT onto the CBD buffer layer. We shall first consider the initial step of the process, drop coating to form a thin ZnO seed layer.

3.1. Effect on the Seed Layer. Figure 1a shows FE-SEM images of a ZnO seed layer prior to CBD growth. It has been shown that these thin films are comprised of small ZnO crystallites which are preferentially orientated with their *c*-axis perpendicular to the substrate.²¹ While this natural orientation is the principal origin of the *c*-axis alignment, in subsequent growth steps there are indications that spatial confinement of nanorods during CBD growth also plays a significant role in the orientation of the CBD rods and hence subsequently grown VPT rods. As can be seen in Figure 1b, the initial CBD growth on the seed layers is not perfectly aligned with respect to the substrate. Gaps in the CBD-grown film cause the nanorods to tilt with respect to substrate, while in areas of increased nanorod density the rods appear better aligned. Similar observations have been made before by Lee et al.,²² who observed multiple rod nucleation occurring in chemical bath depositions when the density of nucleation sites on the substrate was reduced, which lead to poor rod alignment and even misorientation. In fact, for high spatial density CBD nanorod samples, we have even identified occasional rods whose long axis, although normal to the substrate, is not the crystal *c*-axis (Supporting Information, Figure S2). This is a clear indication that the spatial confinement effects on CBD grown rods has important implications for the VPT growth on CBD derived layers, as discussed later. The origin of the rods growing along different crystal orientations is easily understood. The drop coating seeding step is a stochastic process, with zinc hydroxide crystallites forming randomly in the zinc acetate solution and precipitating onto the substrate surface. Subsequently, during annealing the hydroxide precipitate decomposes to form hexagonal ZnO flat platelet-type seeds in a textured layer on the substrate with the *c*-axis predominantly normal to the substrate. However, some variation remains in

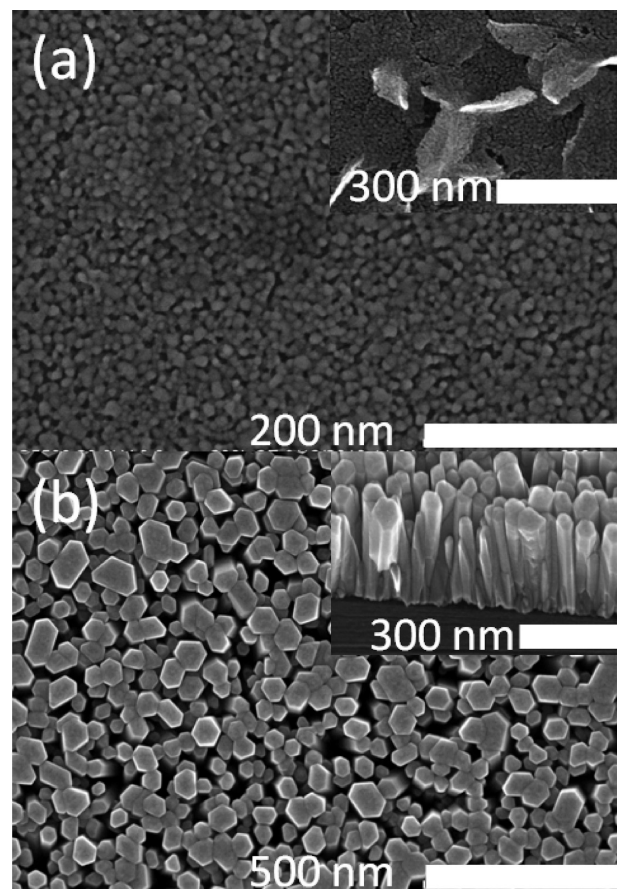


Figure 1. FE-SEM images of (a) drop coated seed layer prior to CBD growth at the sample center (inset: drop coated seed layer at substrate edge where seed density is greatest). (b) Plan view of ZnO nanorods grown by hexamine CBD method (inset: 30° view of ZnO nanorods grown by hexamine CBD method).

both the thickness and degree of *c*-axis alignment of the seed layer crystals because of the overlapping of seeds, especially in areas of increased seed density. The effect can be likened to dropping a deck of playing cards on a flat surface. The majority of cards will lie flat, but some overlapping and tilting will be seen where many cards land in the same region. This can clearly be seen in Figure 1a and the inset, where FE-SEM images of the seed layer from the sample center (where the seed density is lower) and edge (with higher seed density), respectively, show significant variations in thickness, tilt, and uniformity. In combination with spatial confinement effects, the majority of CBD grown rods are forced to grow with the fastest developing crystal axis perpendicular to the substrate, that is, the (0001) axis. However, due to the random overlapping of crystallites in the seed layer, some nucleation sites have *c*-axis so misaligned with respect to the substrate normal that spatial confinement effects are overcome and growth along other crystal orientations becomes possible.

Previously we reported that the thin drop coated ZnO seed layer on silicon was unsuitable for high temperature deposition.²⁰ Growth was principally confined to the substrate edges, with little or no growth occurring on the center of the substrate. Atomic force microscopy (AFM) analysis, as shown in the Supporting Information in ref 20 indicated that during the thermal cycle of the VPT process, this seed layer undergoes a significant modification, the mechanisms of which were unclear. To clarify the

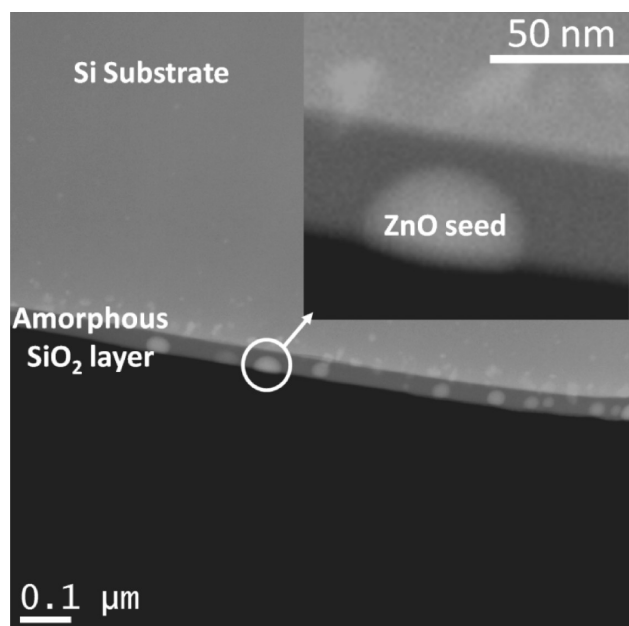


Figure 2. HAADF-STEM image of a drop-coated seed layer annealed using FRTP (insert: higher magnification HAADF-STEM showing an original crystallite imbedded in the surface SiO_2).

processes leading to the alteration of this seed layer, HAADF-STEM (as shown in Figure 2) was performed on a seed layer that was annealed without source material in the furnace using the fast ramp temperature profile (FRTP; See Supporting Information, Figure S1).

A clear transformation is seen in the seed layer from the drop coating process as the small seed crystals become embedded in the amorphous interface. During the high temperature treatment, there is an overgrowth of the seeds by the SiO_2 layer (as confirmed below). It is well-known that at high temperatures silicon wafers can be oxidized, forming much thicker oxide layers than the native oxide present. This growth in thermal oxide is sufficient to encapsulate the small seed crystals rendering them inactive for nanorod nucleation. This suggests that the buffer layer must have a minimum particle size/thickness during VPT deposition, to prevent the SiO_2 overgrowth inhibiting the ZnO nucleation process. Furthermore, the size of the particles embedded in the substrate in Figure 2 suggests crystal coalescence may also be taking place since the sizes of the particles are significantly larger than those previously reported.^{20,21} This phenomenon can also be seen in the FE-SEM image shown in the Supporting Information Figure S3, where individual particles cannot be resolved as they are subsurface features but a clear contrast in the image identifies the embedded particle position. Energy-dispersive X-ray (EDX) analysis of these seeds shows the composition as a $\text{Zn}_x\text{Si}_{1-x}\text{O}_y$ mixing. While the silicon signal is unavoidable due to the small particle size of the embedded seeds, it cannot be ruled out that the seeds also undergo a chemical reaction forming a $\text{Zn}_x\text{Si}_{1-x}\text{O}_y$ type compound at high temperatures as similar reactions have been observed before.²³ For ease of description $\text{Zn}_x\text{Si}_{1-x}\text{O}_y$ will be used in the remainder of the discussion to refer to the mixed oxide interfaces composed of ZnO and SiO_2 .

3.2. Growth of Aligned ZnO Nanorod by CBD. The many factors that affect the final morphology of CBD grown nanorods have been discussed extensively elsewhere^{22,24,25} and are

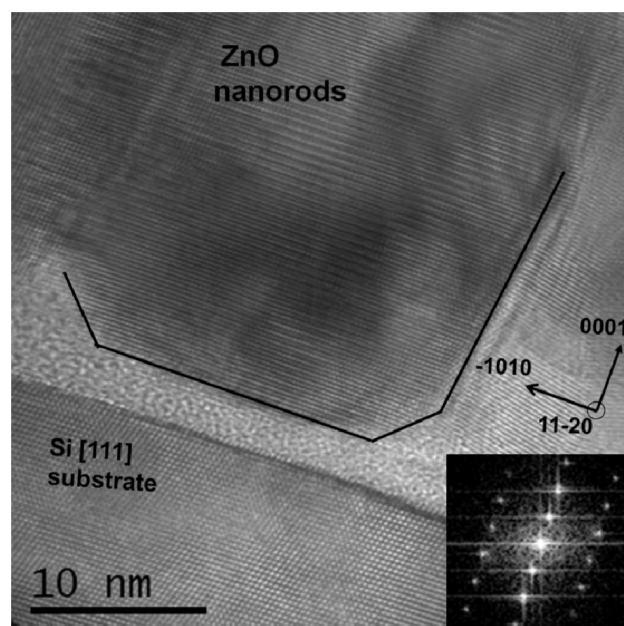


Figure 3. HRTEM image of CBD grown nanorod showing the amorphous SiO_2 interface (insert: Its corresponding fast Fourier transform (FFT) confirming growth direction and wurtzite structure).

therefore not the focus of our work. However, the interface between the CBD deposited nanorods and the drop-coated seed layer was examined by HRTEM to further understand the growth process and subsequent changes that occur during CBD growth. Between the base of the nanorods and the silicon substrate, there is a layer composed in part of amorphous silica (as demonstrated later) formed from the silicon native oxide, as seen in Figure 3.

From the very base of the CBD nanorods, the crystalline quality is good and no significant evidence of structural defects is noticed. The HRTEM image and its corresponding FFT shown in Figure 3 prove the rods have hexagonal structure and are principally growing along the *c*-axis (0001 direction). Similar crystal quality is observed at the base and tip of the rods. In general, it appears as if the nanorods “sink” slightly into the silica layer; however, this is more likely due to slight etching and redeposition of the SiO_2 layer in between nanorods during the CBD growth as the silica interface is somewhat soluble in the basic reaction solution. The CBD nanorod growth begins with a narrow diameter, typically around 15 nm, probably corresponding to the diameter of a single underlying seed particle. In the early stages of growth, the rod diameter increases. This transition occurs within the first 10 nm of growth. This can also clearly be seen in the FE-SEM images shown in Figure 1b. The increase in diameter at the base of the rod is related to the initial conditions of the chemical bath. Previously, it has been recognized that the degree of solution supersaturation influences the morphology of ZnO crystals grown by CBD via the nucleation mechanism.²³ At low supersaturation levels the growth process is dominated by heterogeneous nucleation leading to lateral growth, while at higher supersaturation growth is dominated by the homogeneous nucleation leading to crystal elongation. Given that the seeded substrates were submerged in the reaction solution prior to heating, the initial rod diameter increase is attributed to the initially low zinc hydroxide saturation. Following the CBD growth on the seed buffer layer, a nanorod density

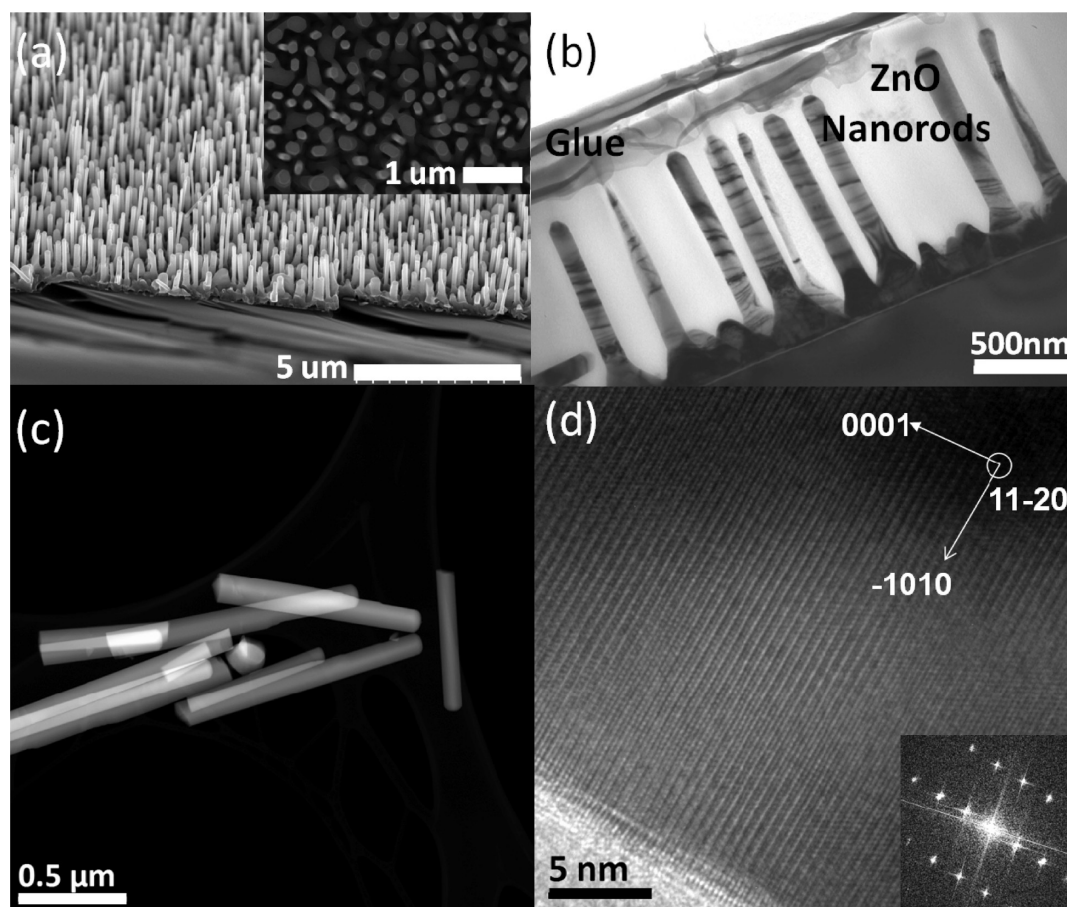


Figure 4. (a) FE-SEM image of a VPT grown nanorod array via FRTP on a CBD buffer layer. (b) TEM image of a sample grown in an identical fashion. (c) HAADF-STEM of VPT grown nanorods scraped from the substrate surface. (d) HRTEM and its corresponding FFT of a single VPT grown nanorod confirming *c*-axis orientation and wurtzite structure.

of $\sim 2 \times 10^{10}$ to $4 \times 10^{10} \text{ cm}^{-2}$ is obtained, a lower value compared to the seed density of $\sim 3 \times 10^{11}$ to $8 \times 10^{11} \text{ cm}^{-2}$, due to the large nanorod diameter compared to the seed diameter.

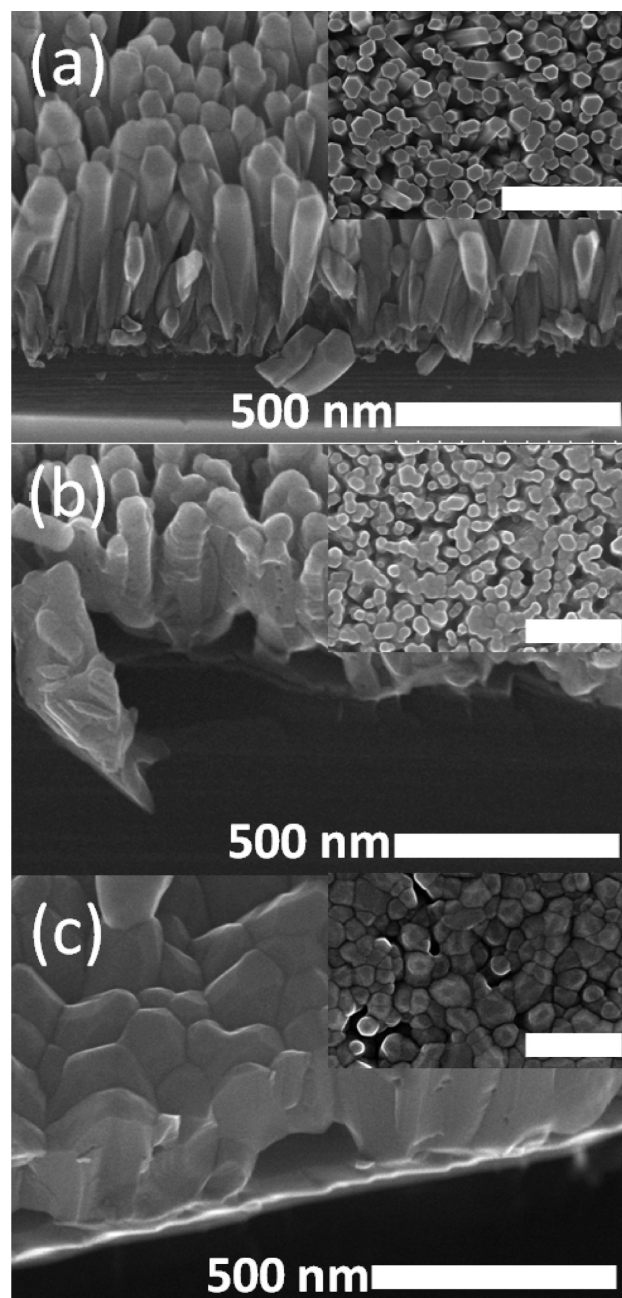
3.3. Morphological Changes of the CBD Buffer Layer during the VPT Deposition. We now consider the final step of the process, the VPT deposition of nanorods on the CBD buffer layer. Typically this was performed using the furnace FRTP (Supporting Information, Figure S1). FE-SEM analysis as shown in Figure 4a, demonstrate that the nanorods grow perpendicular to the substrate, following the alignment of the underlying CBD buffer layer, likewise HRTEM image and corresponding FFT (Figure 4d) confirm the high quality of the material, the wurtzite structure and *c*-axis orientation of the nanorods. HAADF-STEM analysis of material scrapped from the substrate surface (Figure 4c) reveals that the nanorod compositions are uniform along their lengths. The length and diameter of the nanorods varies from sample to sample but are typical $1\text{--}3 \mu\text{m}$ in length with diameters distributed around 100 nm . An important fact is the reduction of the number of nanorods that emerges from the CBD buffer layer. Quantitatively, the VPT nanorod density reduces from 2×10^{10} to $4 \times 10^{10} \text{ cm}^{-2}$ to 2×10^8 to $5 \times 10^8 \text{ cm}^{-2}$, that is, 2 orders of magnitude less than the CBD nanorod density. The VPT nanorods not only increase in diameter but also in the average rod-to-rod distance. The origin of the reduction in rod density is now examined in terms of the role of the buffer layer.

The VPT growth process significantly affects both the base of the VPT grown nanorods and the underlying CBD buffer layer. First, as can be seen in the TEM image in Figure 4b, the base of the nanorods consist of cones which are formed by the fusion of several CBD nanorods and covered with ZnO during the VPT deposition. During the VPT growth Zn vapor is deposited oxidized to form ZnO which fills the gaps between neighboring CBD nanorods in the buffer layer giving rise to only one nanorod which emerges from the conical base. The conical bases change depending on both the temperature ramp rate and the position of the substrate with respect to the source material. At the slow ramped temperature profile (SRTP), the conical base height extends (in length) much further up the rod than the original CBD rod height, but significantly, only a minor increase in the base diameter is also observed with respect to CBD objects. Second, when the substrate is closer to the source powder, using the FRTP, the conical base appears a lot wider at the bottom and longer as compared to other samples prepared using FRTP with substrates further from the source powder. This suggests that the temperature profile influences the change in growth conditions from 2D to 1D, which is consistent with other reports on the effect of temperature ramp on VPT growth.²⁶

Table 1 summarizes the morphological variations in the conical base observed for the different temperature profiles. While the growth parameters have an influence on the base of the structures, no significant variation in the diameter of final

Table 1. Variation in Conical Base Width and Height for Samples Grown with Varying Conditions

growth conditions	height (nm)	width (nm)
FRTP	260 ± 40	340 ± 60
FRTP with the substrate placed close to the source powder	510 ± 90	400 ± 70
SRTP	500 ± 45	125 ± 50

**Figure 5.** FESEM images of a CBD buffer layer (a) 30° view (inset: plan view) prior to annealing, (b) post annealing using SRTP (inset: plan view), (c) post annealing using FRTP (inset: plan view). Scale bar in all images is 500 nm.

VPT nanorods has been observed. Li et al. reported that both the buffer layer surface roughness and the crystallinity affect the

nucleation of nanorods during VPT growth on PLD deposited buffer layers.¹⁵ When the surface roughness was small, an intermediate continuous network was formed. With higher surface roughness, the diffusion of zinc vapor across the surface is reduced and no obvious continuous network was formed. While some evidence of intermediate network formation can be seen in our samples (Supporting Information, Figure S4), rods also appear to grow directly from the CBD nanorods with conical bases. The origin of the variation in intermediate network formation versus conical base formation is not explicitly clear. While the network formation may result from overlapping conical bases, it may also be due to favorable nucleation ridges in the CBD buffer layer, leading to wall like structures during the high vapor saturation levels achieved in the initial stages of VPT growth. Furthermore, varying the number of drop coats, which in turn varies the CBD buffer layer density, does not appear to significantly enhance or reduce the intermediate network formation. The nucleation process is further complicated by the fact that the CBD buffer layer undergoes substantial morphological changes during VPT growth.

To further understand what happens to the CBD buffer layer during VPT growth, CBD buffer layers were annealed in conditions identical (but without Zn source material) to those used for the VPT deposition using both FRTP and SRTP. FE-SEM images before and after annealing can be seen in Figure 5.

Prior to annealing, the CBD buffer layer consists of distinct hexagonal shaped nanorods, approximately 350 nm long. Post annealing using SRTP conditions, many of the rods have fused with neighboring rods forming thicker irregular shaped structures. The lateral facets of the rods appear rougher as compared to their unannealed counterparts. In addition, clearly faceted voids appear in the base of the CBD film. At the faster temperature ramp rate FRTP, the films undergo an even more dramatic transformation. The hexagonal faceting of individual rods are not visible, with only a granular fused film remaining. The lateral facets can no longer be observed accurately as all the rods have substantially deformed. Thermal stress cracks formed during sample cooling are also observed, indicating the complete fusion of the CBD film. Faceted voids in the buffer layer are also clearly visible and are regularly found both in VPT grown samples and SRTP annealed buffer layers. Thus, at high temperatures, the annealed layer of CBD deposited rods undergoes a transformation from hexagonal-shaped rods to a diamond-like shape, with occasional faceted voids between structures, examples of which are shown in the Supporting Information (Figure S5) and Figure 6b. This transformation might be due to partial sublimation of the ZnO buffer and its transport along the wire length. It has been known for quite some time that the chemical etching and sublimation rate of ZnO varies between the different faces of the ZnO crystal due to the anisotropic nature of the wurtzite crystal.^{27,28} In addition, the presence of surface adsorbed impurities such as water can vary the surface free energy, further altering the initial sublimation rate of the different crystal faces.²⁷ While Leonard et al.²⁷ ascribed attenuated initial sublimation rates of ZnO at high temperatures to surface adsorbed impurities such as water. Ntep et al.²⁹ found that the presence of water in the gaseous mixture actually assisted the sublimation process. Given that the buffer layers are grown in solution, water and other surface impurities are undoubtedly present. In either case, what is clear is that the various facets of ZnO can undergo sublimation at different rates and that the reported temperatures necessary for sublimation to occur are achieved in our experiments. Although

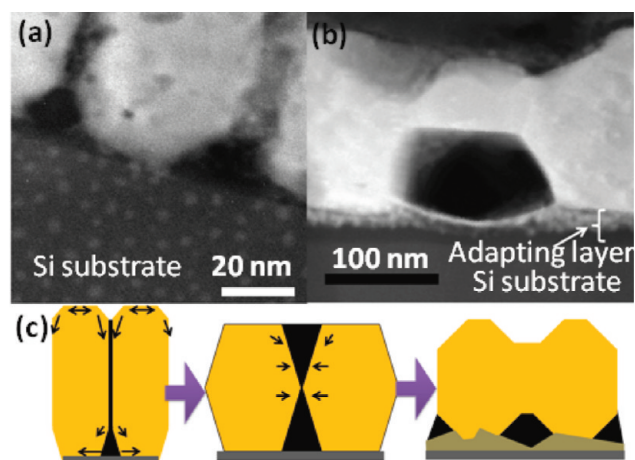


Figure 6. HAADF-STEM images of (a) the base of a CBD nanorod prior to VPT deposition, (b) of a faceted void formed in an annealed CBD buffer layer, (c) schematic representation of the diffusion of material along the CBD buffer layer during VPT growth/annealing.

the changes seen during annealing are instructive in terms of understanding the origin of effects seen during VPT growth, we do note, in relation to sublimation processes, that during the VPT process, the higher vapor pressure coming from the source limits the sublimation yield, and as a result this may restrict the morphological changes on the original CBD nanorod compared to the annealing process. To compound the complexity of the structural transformations observed, it has been reported that ZnO nanostructures can have melting temperatures well below that of the bulk material.^{30–32} At present, this phenomenon is poorly understood. Using the theoretical model put forward by Guisbiers et al.,³³ using the maximum and minimum differences between the surface tensions in the liquid and solid phases ($(\gamma_l - \gamma_s) = \max/\min$ value) yields a predicted melting temperature range of 1764–1883 °C for hexagonal nanorods with a 20 nm side length and height of 300 nm, well above the temperatures reached during our experiments. However, partial melting cannot be completely ruled out as the cause of the structural transformations and faceted void formation, as other reports have indicated that nanoparticles can melt at temperatures significantly lower than those predicted by Guisbiers's model.³⁰ Regardless of the precise microscopic mechanism, the key point is that the material moves from the upper basal facet and prismatic facets of the nanorod and deposits on the pyramidal facets during VPT growth/annealing, creating diamond-shaped structures, leading to the partial fusing of several wires. As the material transport also happens during annealing where no additional zinc source vapor is being provided, it must be the case that an important aspect affecting the increase in rod diameter during VPT growth must be from material already present, that is, material redistribution as discussed above. The fused CBD rods provide a wider base on which the subsequent VPT deposition and coverage occur to create the conical bases. Depending on the supersaturation levels in the VPT step, the growth mode reverts back to 1D more or less quickly, thus affecting the shape of the cone at the base of the nanorods. Despite the conflicting reports on the influence of melting on ZnO nanostructures at temperatures less than bulk values, we believe rather that this transformation is primarily due to the partial sublimation, transport, and redeposition of the ZnO in the nanorods because a similar effect is observed at the base of the CBD rods.

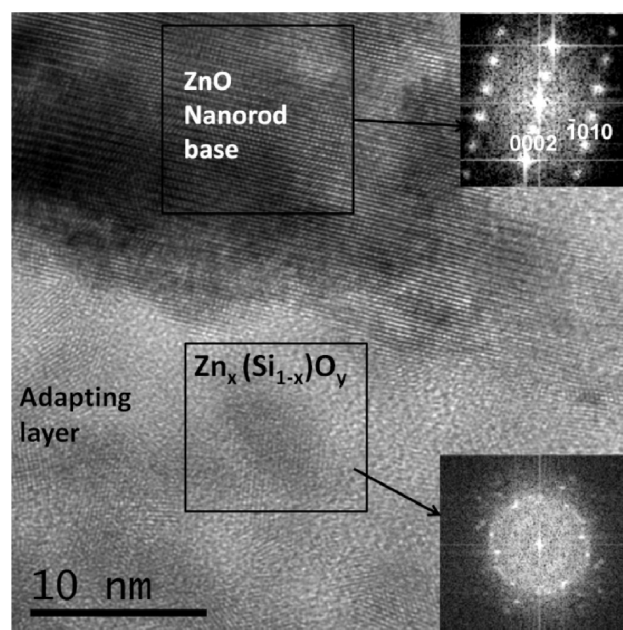


Figure 7. HRTEM of a VPT grown sample at the SiO₂-ZnO interface and corresponding FFT of the SiO₂ and ZnO regions.

Sharp faceted edges have been seen at the interface between the SiO₂ and the nanorod bases, which is not seen prior to high temperature treatments (compare Figure 6, panels a and b), which would suggest that the interface is formed by the diffusion of zinc vapor rather than the transport of material by amorphous liquid droplets. During annealing, ZnO is also removed from planes of the rod base and subsequently diffuses into the silica interface layer, as shown by the schematic in Figure 6c.

The thermal induced structural transformation is clearly also responsible for the void formation. During VPT growth or annealing, the newly forming diamond-like rods can come into contact with neighboring rods and fuse along their sides, creating faceted caverns in the buffer layer. As a consequence, the formation of voids in the buffer layer during VPT growth is dependent on the density of the CBD deposited buffer layer prior to growth, which in turn is dependent on the number of drop-coats used to prepare the seed layer and the growth conditions during the CBD deposition step.^{25,34}

3.4. Effect on the Adapting Layer. In our experiments, the ZnO was initially grown by CBD on silicon, without removing the native oxide. The intermediate layer between the CBD rods and the substrate (Figure 3) indicate that the smooth native oxide is not significantly disturbed by the CBD process. Consequently, the bases of the CBD nanorods are generally flat with respect to the native oxide and are of good crystalline quality. Nevertheless, after VPT growth or any annealing process the nature of this intermediate layer changes becoming thicker and being composed of two different regions with three distinct interfaces. HRTEM micrographs of the SRTF rod/adapting layer interface and corresponding FFT reconstructions confirm a good crystalline quality in the onset of rod growth. More importantly, the FFT of the adapting layer (see Figure 7) also yields a weak diffraction pattern implying the formation of a mixture of crystalline phases in this amorphous region, as detailed below.

The two layers that make up the adapting layer were examined by EELS and EDX. EDX analysis of a profile across the adapting

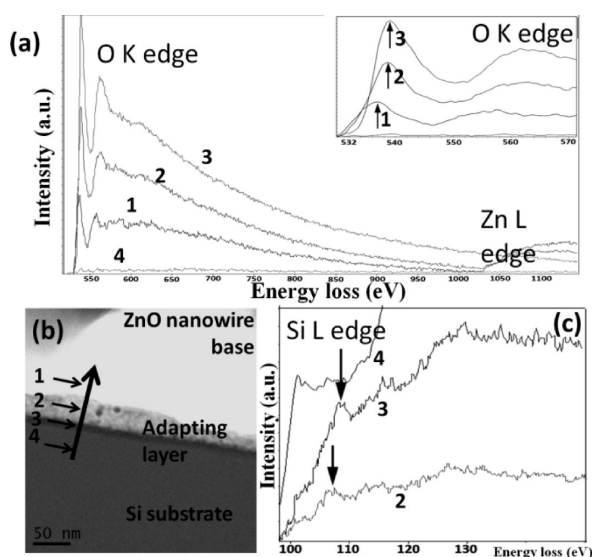


Figure 8. (a) Individual core loss EEL spectra from several points at the Si substrate/wires interface, which are labeled in (b), HAADF-STEM image of this region. The points 1–4 correspond to ZnO wire base, $\text{Zn}_x\text{Si}_{1-x}\text{O}_y$, SiO_2 layers and Si substrate, respectively. (c) Low loss spectra of this same region exhibiting different Si-L signals.

layer from the substrate shows that zinc is not the dominant component, but amorphous SiO_2 . The individual spatially resolved EEL spectra across the interface (Figure 8a) display the characteristic signal of the Zn-L and O-K edges. First, they indicate that a sharp interface between the silicon and SiO_2 exists, which is also clearly visible in the HAADF-STEM image in Figure 8b. From the SiO_2 layer (indicated as 3 in Figure 8a), the oxygen signal gradually decreases until it has reached a steady value corresponding to the onset of the ZnO nanorod (point 1). The Zn-L signal begins before the O-K signal has reached this steady state (see point 2) suggesting that either just the base of the nanorod is oxygen-rich compared to the bulk of the rod or that the area also contains a significant amount of other oxygen containing species. Thus, when scanning the sample from the substrate to the ZnO base, the Zn-L edge signal does not vary significantly but the O-K signal of the recorded spectra does experience a progressive red-shift in the adapting layer. This can be better appreciated by following the arrows which mark the energy of the oxygen edges at each layer. In addition, the Si-L signal taken at the same area also undergoes a strong signal modification between the Si substrate and the adapting layer (see Figure 8c) (point 4 compared with the others) and moreover a slight peak change with decreasing energy when comparing the two sublayers defined inside the adapting area (point 2 with respect to point 3). These results suggest that the area observed is something more than ZnO polycrystalline particles immersed in an amorphous SiO_2 matrix and that new zinc silicate species could have been formed where the oxidation state of Si and Zn atoms remains constant. In the literature, we have found up to three different compounds combining Zn–Si–O.³⁵ Nevertheless, the accepted phase diagram of ZnO– SiO_2 only considers the thermodynamically stable intermediate compound Zn_2SiO_4 (Willemite), which melts congruently at 1512 °C and forms two eutectics with SiO_2 and with ZnO.³⁶ Hence, the most probable compound is Zn_2SiO_4 , which can be formed at 770 °C. Furthermore, FFT reconstruction of HRTEM images

for several SiO_2 –ZnO interfaces reveal the existence of intense spots with interplanar spacing in agreement with the values for Zn_2SiO_4 crystals. On the basis of these results, we propose that a mixed crystal of ZnO, SiO_2 , and Zn_2SiO_4 occurs in this region. Similar results of the mixed formation of Zn_2SiO_4 crystal and amorphous SiO_2 during annealing treatments have been reported in annealed ZnO/Si systems.³⁷ Taking into account all the EELS and HRTEM data, we conclude that the adapting layer follows this stacking sequence: Si / SiO_2 / Zn_2SiO_4 – ZnO immersed in SiO_2 / ZnO.

The amorphous adapting layer has also been observed for samples annealed without VPT growth, indicating that the presence of Zn in the adapting layer is not solely due to Zn vapor from the carbothermal reduction reaction. In fact, the close similarity between samples either annealed or following VPT growth indicates that the main source of Zn in the adapting layer is probably due to a partial consumption of the CBD deposited rods into the interface. With this in mind, it is interesting to note that there are some differences observed in the adapting layers between samples grown by VPT at both temperature ramp rates and those by CBD followed by annealing using the FTRP, a comparison of which is shown in the Supporting Information (Figure S6). The interface layer of samples annealed is significantly rougher than those grown by VPT. The most uniform interface layer is achieved with the lower temperature ramp rate, thus optimizing the interface between the substrate and the rod. The thickest interface layer occurs in samples grown by VPT with the FTRP. This is attributed to the higher temperatures achieved from the beginning of the step, which in turn leads to a more rapid growth of the ZnO/ SiO_2 adapting layer. The most uneven adapting layers are observed in the samples annealed without the source powder suggesting that the Zn vapor has a moderating effect on the oxygen partial pressure leading to a more uniform growth of the SiO_2 interface. The most uniform adapting layers were obtained using the STRP.

The complex adapting layer under the bases of the hexagonal ZnO nanorods has been discovered to be a mixed phase that includes a ternary compound of the Zn silicate type. Our results indicate that a significant atomic diffusion between the ZnO film and the silicon substrate occurs during high temperature growth by VPT process or annealing above 800 °C. The exact consequences of the formation of this complex interlayer between the silicon substrate and the nanorod array and its impact on these structures potential use in future devices is beyond the focus of this work. Furthermore, there have been as yet, to our knowledge, few studies devoted to this topic. Consequently, further studies are needed to elucidate exactly how this layer will affect both the electrical and optical properties of nanorods grown by the present method.

4. CONCLUSIONS

In this work, we have studied VPT deposition of high quality ZnO nanorods on CBD buffer layers and the effects of the growth process on the seed and buffer layers. Thin drop-coated ZnO seed layers on silicon are unsuitable for direct high temperature deposition because the small seeds from the drop coating process suffer a transformation by becoming embedded in the SiO_2 interface leading to an overgrowth of the seeds by the SiO_2 layer, clearly indicating that there is a critical particle size and/or film thickness necessary for the aligned growth of ZnO nanorods by VPT at high temperatures. The buffer layer also undergoes

significant transformations including structural changes which, in conjunction with different Zn vapor pressures and furnace temperatures, lead to the formation of conical nanorod bases in a complex interplay of competing factors. These bases are formed via fusion of several CBD nanorods giving rise to a single high quality nanorod which emerges from this conical base. Consequently, a reduction in the ultimate nanorod density occurs with respect to the original CBD nanorod density. Despite a degree of residual uncertainty in terms of the microscopic processes involved in sublimation and melting, the outcomes from high temperature annealing treatments suggest that the origin of the structural changes in the buffer layer comes from partial sublimation during high temperature growth. Finally, the adapting layer between the substrate and the buffer layer also changes during high temperature growth, forming two distinct regions separated by sharp interfaces with the sequence Si / SiO₂ / ZnO-Zn₂SiO₄-SiO₂ / ZnO. This is a particularly important factor if ZnO nanorods grown by VPT are to be incorporated into electronic devices, where the substrate is expected to function as an electrical contact to the nanorod also.

■ ASSOCIATED CONTENT

S Supporting Information. Experimental: description of the growth processes used in this work, including the drop-coating, CBD and VPT steps. Figure S1: Furnace temperature profiles used for the various VPT depositions on CBD buffer layers. Figure S2: HR-TEM and corresponding FFT of a CBD deposited nanorod, growing along the (10 $\bar{1}$ 0) axis. Figure S3: Plan view FE-SEM image of a drop-coated seed layer annealed using FRTP. Figure S4: Plan view FE-SEM image of a VPT grown sample using FRTP, showing the tops of the nanorods with an intermediate network formation around the base of the rods. Figure S5: 90° view (cross-section) of a cleaved edge of CBD grown sample after high temperature annealing, showing the formation of faceted voids and diamond shaped structures. Figure S6: HAADF-STEM images of (a) FRTP annealed CBD buffer layer showing rough and nonuniform interface, (b) FRTP VPT deposited nanorods on CBD buffer layer showing conical base and more uniform interface layer, (c) SRTP deposited nanorods on CBD buffer layer showing a very uniform interface layer. This material is available free of charge via the Internet at <http://pubs.acs.org>.

■ AUTHOR INFORMATION

Corresponding Author

*E-mail: daragh.byrne2@mail.dcu.ie.

■ ACKNOWLEDGMENT

Financial support from Spanish Project CICYT MAT2010-15206 is gratefully acknowledged. D.B. and E.M.C.G. acknowledge support from Science Foundation Ireland Strategic Research Cluster grant entitled “Functional Oxides and Related Materials for Electronics” (FORME). B.T. would like to acknowledge financial support from SFI (equipment funding under Grant No. 03/IN3/1361/EC07).

■ REFERENCES

- Banerjee, A. N.; Nandy, S.; Ghosh, C. K.; Chattopadhyay, K. K. *Thin Solid Films* **2007**, *515* (18), 7324–7330.
- Ling, B.; Sun, X. W.; Zhao, J. L.; Tan, S. T.; Dong, Z. L.; Yang, Y.; Yu, H. Y.; Qi, K. C. *Phys. E* **2009**, *41* (4), 635–639.
- Wang, J. X.; Sun, X. W.; Yang, Y.; Huang, H.; Lee, Y. C.; Tan, O. K.; Vayssieres, L. *Nanotechnology* **2006**, *17* (19), 4995–4998.
- Rout, C. S.; Hari Krishna, S.; Vivekchand, S. R. C.; Govindaraj, A.; Rao, C. N. R. *Chem. Phys. Lett.* **2006**, *418* (4–6), 586–590.
- Law, M.; Greene, L. E.; Johnson, J. C.; Saykally, R.; Yang, P. D. *Nat. Mater.* **2005**, *4* (6), 455–459.
- Mane, R. S.; Lee, W. J.; Pathan, H. M.; Han, S.-H. *J. Phys. Chem. B* **2005**, *109* (51), 24254–24259.
- Garry, S.; McCarthy, E.; Mosnier, J. P.; McGlynn, E. *Appl. Surf. Sci.* **2011**, *257* (12), 5159–5162.
- Lin, C.-C.; Li, Y.-Y. *Mater. Chem. Phys.* **2009**, *113* (1), 334–337.
- Lu, C.-H.; Yeh, C.-H. *Ceram. Int.* **2000**, *26* (4), 351–357.
- Greene, L. E.; Law, M.; Goldberger, J.; Kim, F.; Johnson, J. C.; Zhang, Y. F.; Saykally, R. J.; Yang, P. D. *Angew. Chem. Int. Ed.* **2003**, *42* (26), 3031–3034.
- Sun, Y.; Fuge, G. M.; Ashfold, M. N. R. *Chem. Phys. Lett.* **2004**, *396* (1–3), 21–26.
- Grabowska, J.; Nanda, K. K.; McGlynn, E.; Mosnier, J. P.; Henry, M. O. *Surf. Coat. Technol.* **2005**, *200* (1–4), 1093–1096.
- Li, Z. Y.; Xu, F. C.; Wu, Q. H.; Li, J. *Appl. Surf. Sci.* **2008**, *255* (5), 2859–2863.
- Panchakarla, L. S.; Shah, M. A.; Govindaraj, A.; Rao, C. N. R. *J. Solid State Chem.* **2007**, *180* (11), 3106–3110.
- Li, C.; Fang, G. J.; Li, J.; Ai, L.; Dong, B. Z.; Zhao, X. Z. *J. Phys. Chem. C* **2008**, *112* (4), 990–995.
- Li, C.; Fang, G.; Fu, Q.; Su, F.; Li, G.; Wu, X.; Zhao, X. *J. Cryst. Growth* **2006**, *292* (1), 19–25.
- Park, D. J.; Kim, D. C.; Lee, J. Y.; Cho, H. K. *Nanotechnology* **2006**, *17* (20), 5238–5243.
- Kang, D.-S.; Han, S. K.; Kim, J.-H.; Yang, S. M.; Kim, J. G.; Hong, S.-K.; Kim, D.; Kim, H.; Song, J.-H. *J. Vac. Sci. Technol. B* **2009**, *27* (3), 1667–1672.
- Byrne, D.; McGlynn, E.; Henry, M. O.; Kumar, K.; Hughes, G. *Thin Solid Films* **2010**, *518* (16), 4489–4492.
- Byrne, D.; McGlynn, E.; Kumar, K.; Biswas, M.; Henry, M. O.; Hughes, G. *Cryst. Growth Des.* **2010**, *10* (5), 2400–2408.
- Greene, L. E.; Law, M.; Tan, D. H.; Montano, M.; Goldberger, J.; Somorjai, G.; Yang, P. D. *Nano Lett.* **2005**, *5* (7), 1231–1236.
- Lee, Y. J.; Sounart, T. L.; Liu, J.; Spoecker, E. D.; McKenzie, B. B.; Hsu, J. W. P.; Voigt, J. A. *Cryst. Growth Des.* **2008**, *8* (6), 2036–2040.
- Lim, Y. S.; Park, J. W.; Kim, M. S.; Kim, J. *Appl. Surf. Sci.* **2006**, *253* (3), 1601–1605.
- Saeed, T.; O'Brien, P. *Thin Solid Films* **1995**, *271* (1–2), 35–38.
- Govender, K.; Boyle, D. S.; Kenway, P. B.; O'Brien, P. *J. Mater. Chem.* **2004**, *14* (16), 2575–2591.
- Kumar, R. T. R.; McGlynn, E.; McLoughlin, C.; Chakrabarti, S.; Smith, R. C.; Carey, J. D.; Mosnier, J. P.; Henry, M. O. *Nanotechnology* **2007**, *18* (21), 215704.
- Leonard, R. B.; Searcy, A. W. *J. Appl. Phys.* **1971**, *42* (10), 4047.
- Iwanaga, H.; Yoshiie, T.; Yamaguchi, T.; Shibata, N. *J. Cryst. Growth* **2007**, *303* (5–6), 703–711.
- Ntep, J. M.; Barbé, M.; Cohen-Solal, G.; Bailly, F.; Lusson, A.; Triboulet, R. *J. Cryst. Growth* **1998**, *184*–185, 1026–1030.
- Su, X.; Zhang, Z. J.; Zhu, M. M. *Appl. Phys. Lett.* **2006**, *88* (6), 061913.
- Yan, Z.; Ma, Y.; Wang, D.; Wang, J.; Gao, Z.; Wang, L.; Yu, P.; Song, T. *Appl. Phys. Lett.* **2008**, *92* (8), 081911–081911–081913.
- Yan, Z.; Zhu, K.; Chen, W. P. *Appl. Phys. Lett.* **2008**, *92* (24), 241912.
- Guisbiers, G.; Pereira, S. *Nanotechnology* **2007**, *18* (43), 435710.
- Lee, Y. J.; Sounart, T. L.; Scrymgeour, D. A.; Voigt, J. A.; Hsu, J. W. P. *J. Cryst. Growth* **2007**, *304* (1), 80–85.

- (35) Xu, X.; Guo, C.; Qi, Z.; Liu, H.; Xu, J.; Shi, C.; Chong, C.; Huang, W.; Zhou, Y.; Xu, C. *Chem. Phys. Lett.* **2002**, 364 (1–2), 57–63.
- (36) Jak, E.; Degterov, S.; Wu, P.; Hayes, P. C.; Pelton, A. D. *Metall. Mater. Trans. B* **1997**, 28 (6), 1011–1018.
- (37) Xu, X. L.; Wang, P.; Qi, Z. M.; Ming, H.; Xu, J.; Liu, H. T.; Shi, C. S.; Lu, G.; Ge, W. K. *J. Phys.: Condens. Matter* **2003**, 15 (40), L607–L613.